Determining Beam Bending Distribution Using Dynamic Information

Frank G. Polanco

DSTO-RR-0226

20020226 084

Determining Beam Bending Distribution Using Dynamic Information

Frank G. Polanco

Airframes and Engines Division
Aeronautical and Maritime Research Laboratory

DSTO–RR–0226

ABSTRACT

As a first approximation, a helicopter rotor blade may be modelled as a cantilever beam. Given the initial deformation of this beam, and using either strain or acceleration at one location along the beam, we can determine the load distribution along the entire beam. We consider load distributions that can vary spatially, but are constant in time (except for the initial step input). In the solution we neglect the effects of both aerodynamic and mechanical damping. The separation of variables technique leads to a solution in terms of the beam's natural modes. The loading distribution is decomposed in terms of these modes. A finite element simulation of the beam's response to a cubic load distribution verifies that this load prediction is possible. We demonstrate that the higher modes of the load prediction are unstable when noise is present in the measurements, but that the lower modes are robust. If the initial beam deformation is unknown, then additional (strain or vibration) measurement locations may be substituted for the unknown initial deformation.

APPROVED FOR PUBLIC RELEASE

DEPARTMENT OF DEFENCE
DEFENCE SCIENCE & TECHNOLOGY ORGANISATION

DSTO

AQ F02-05-0829

APPROVED FOR PUBLIC RELEASE

Determining Beam Bending Distribution Using Dynamic Information

EXECUTIVE SUMMARY

In service, helicopter rotor blades undergo a load distribution that is currently not measured; yet this loading distribution determines the fatigue life of a blade. Given that the rotor blades are critical components in helicopters, this lack of information has safety implications. Currently, to maintain a conservative safety factor rotor blades are necessarily retired well before their usage life has been consumed. Accurately predicting the load distribution on a helicopter rotor blade has the potential to both increase safety and reduce operating costs. In this report, we use the vibration of the rotor blade to determine the loading distribution along the blade.

The rotor blade is modelled as a simple cantilever beam (although more general end constraints are possible), and both aerodynamic and mechanical damping are ignored. We begin our load determination analysis with the beam already vibrating due to a previous excitation. Hence, when we begin our analysis the beam already has both an initial deformation and velocity. The unknown load distribution is then applied as a step function, and remains temporally constant after its application. In order to determine the loading distribution, we require the beam's vibration response to this step load. Either strains or accelerations may be used as the beam's vibration response. We show that given the beam's initial deformation and vibration response at only *one* location, it is possible to predict the load distribution along the entire blade.

We use the separation of variables method to write the solution in terms of the blade's natural modes. We then solve for the load distribution in terms of these natural modes. It is not possible to determine both the initial deformation and loading distribution given only the vibration response at one location.

A finite element (FE) model of the beam's response to a step load is used to simulate the strain near the fixed end of the cantilever beam. We use these simulated strain data to predict the load distribution along the FE beam. The simulations verify the load prediction capability outlined, but demonstrate the prediction's susceptibility to measurement noise (especially in predicting higher frequency modes).

If the initial beam deformation is unknown, then additional (strain or vibration) measurement locations may be substituted for knowledge of the initial deformation.

Author

Frank G. Polanco
Airframes and Engines Division

Frank Polanco graduated in 1992 with a Bachelor of Aerospace Engineering (Honours) and a Bachelor of Applied Science (Distinction) from the Royal Melbourne Institute of Technology (RMIT). He joined the Aeronautical and Maritime Research Laboratory (AMRL) in 1993, working on aircraft structural integrity and fatigue life monitoring before returning to RMIT to complete a Doctorate in Mathematics. He then rejoined the AMRL in 1998 to work in the area of helicopter life assessment.

Contents

Figures

Tables

Notation

Roman Symbols		Definition
a	Fourier cosine coefficient	(p. 14)
A	constant from fourth order differential equation	(p. 5)
$\mathcal{A}_j$	constant from jth second order differential equation	(p. 10)
b	Fourier sine coefficient	(p. 14)
B	constant from fourth order differential equation	(p. 5)
$\mathcal{B}_j$	constant from jth second order differential equation	(p. 10)
C	constant from fourth order differential equation	(p. 5)
D	constant from fourth order differential equation	(p. 5)
Δt	time step between temporal samples	(p. 18)
E	Young's modulus	(p. 3)
F	axial load on a beam	(p. 27)
f	distributed force acting along beam	(p. 3)
h	hat function (sum of two step functions)	(p. 12)
i	dummy variable (sometimes used as count for discrete load)	(p. 9)
i	dummy variable (sometimes used as count for Fourier series)	(p. 14)
j	dummy variable (sometimes used as count for series expansion)	(p. 8)
I	beam's cross-sectional area moment of inertia	(p. 3)
K	number of load segments	(p. 9)
l	beam length	(p. 3)
m	beam mass	(p. 3)
n	number of mode shapes in approximating solution	(p. 15)
P	loading period	(p. 13)
t	temporal variable	(p. 3)
t_i	counting variable (for the evaluation of relative errors)	(p. 18)
t_{fin}	final count (number of time evaluations)	(p. 18)
T	temporal variable in separation of variables technique	(p. 5)
v	transverse velocity of beam	(p. 4)
x	horizontal spatial variable (distance along beam)	(p. 3)
y	transverse deformation of beam	(p. 3)
Y	transverse deformation variable in separation of variables	(p. 5)

...notation continued from previous page

Greek Symbols		**Definition**
α	hyperbolic constant: function of β	(p. 5)
β	separation constant: from the separation of variables	(p. 5)
γ	represents series from beam acceleration	(p. 11)
δ	delta (or Kronecker delta) function	(p. 9)
ϕ	coefficient for series expansion of discrete load	(p. 8)
Φ	magnitude of discrete load	(p. 9)
ψ	coefficient of series expansion of vertical deformation	(p. 8)
σ	initial beam deformation decomposed into modes	(p. 14)
τ	initial beam velocity decomposed into modes	(p. 14)
ξ	location of discrete load	(p. 9)
ξ_*	accelerometer or strain gauge location along beam	(p. 11)
ω	loading frequency	(p. 14)

Miscellaneous Symbols
(in the following notation a is a dummy variable)

a_j	denotes the jth solution of the separation of variables	(p. 5)
a_0	initial condition	(p. 4)
$\bar{a}$	dimensional variable	(p. 3)
a'	derivative of a with respect to space, if $a = a(x)$ then $a' = da/dx$	(p. 5)
$\dot{a}$	derivative of a with respect to time, if $a = a(t)$ then $\dot{a} = da/dt$	(p. 5)
$a^{(n)}$	nth derivative of a, if $a = a(x)$ then $a^{(n)} = d^n a/dx^n$	(p. 5)
$\mathcal{O}(a^n)$	of order a^n	(p. 7)
$\hat{a}$	approximation of a	(p. 7)

1   Introduction

Helicopter rotor blades are considered critical components; yet the loading these blades undergo in actual service is largely unknown. Determining the loading distribution history of a helicopter rotor blade has the potential to lead to increased safety. Additionally, because rotor blades are currently retired at a specified component retirement time, these blades may very well have a significant amount of life (at an acceptable level of reliability) remaining. The accurate determination of the in-flight loading distribution on a rotor blade therefore has the potential to save the helicopter operator unnecessary replacement costs.

The approach we use is analogous to determining the load around the rim of a glass given the vibration response of the glass. The glass will ring differently depending on the loading distribution around the rim. For a rotor blade this "ringing" is unique.

In this report we develop a method to determine the load distribution on a cantilever beam (a first order approximation of a helicopter rotor blade). We determine this load distribution using either strain or acceleration measurements at only *one* location along the beam.

Unfortunately we can only determine this loading distribution if we're given the beam's initial deformation. Although we model a rotor blade only as a cantilever beam, a similar analysis may be applied to more generalised end conditions (for example, an end constraint that is a combination of a spring and pin joint).

In the remainder of this introduction (§ 1.1) we will review the literature for similar problems. In § 2 we develop the partial differential equation (PDE) governing the vibration of a cantilever beam. In § 3 we solve this PDE using the well known separation of variables technique. In § 4 we develop the vibration solution for different loading distributions, which include impulse loads, step loads, and a distributed load in terms of the beam's natural modes. In § 5 we perform a simulation, which verifies the theoretical solutions we develop. We then discuss some of the assumptions and findings in § 6 before concluding the report in § 7.

1.1   Review of Beam Vibration

Barcilon [3] determined the elastic properties (that is, stiffness and mass distribution) of a vibrating body using measurement data. As an example a discretised beam was analysed, one end was free and the other end was either free, supported, clamped, or constrained in a non-standard way (we term this end the "constrained" end). An impulse force was applied to the stationary beam at the free end, and the resulting deformation and slope of the constrained end measured. Knowing these deformations and slopes is equivalent to knowing three sets of natural frequencies, which are necessary to infer the elastic properties of the beam. Barcilon refers to these trio of spectra as "sympathetic" spectra. Given these three sympathetic spectra, the solution of the inverse problem, if it exists, is unique. In a later paper, Barcilon [4] investigated an apparent paradox between this uniqueness result and a paper by Boley and Golub [6], who find a multiplicity of solutions when constructing a symmetric pentadiagonal matrix from its spectra. Barcilon

states that beam vibration problems lead to pentadiagonal systems when recast as finite difference problems, and hence the apparent paradox. This apparent paradox is resolved when Barcilon shows that Boley and Golub chose their three spectra without regard for "sympathy" between the spectra.

Gladwell [8] modelled a beam using rigid rods joined together by rotational springs, with lumped masses at the joints. One end of the beam was clamped, while the other end met one of four conditions: free, pinned, sliding, or clamped. Gladwell establishes necessary and sufficient conditions for the existence of a discrete model having a given spectrum, and sets up a procedure to find the model. In a later paper Gladwell [9] reviewed the literature for solutions to inverse vibration problems. Essentially that review looked at the problem of determining the system's properties (for example, mass and stiffness) from vibration measurements.

Berman [5] investigated the problem of system identification using data obtained from dynamic tests of the structure. The structure was modelled by a linear mass, damping, and stiffness matrix. Berman concludes that the most promising approach to modelling is to use test data to minimally modify a realistic analytic model (subject to a set of physical constraints).

Öry, Glaser, and Holzdeppe [22] reconstructed external and internal forces based on measured structural responses. They assumed *a priori* knowledge of the mass distribution and dynamic behaviour of the system, and a linear elastic system with proportional viscous damping. The number of dynamic response measuring locations should be higher than the number of significant modes. They gave an example of a discretised cantilever beam that had several measurement locations along the beam. This work was extended in later papers by one of the above authors [23, 24].

Arosio, Panizzi, and Paoli [2] proved the well-posedness of a Timoshenko beam[1] with axially varying physical properties and sliding ends. They state that the equation cannot be studied using an iteration of the Fourier series, and instead used a variational approach developed by Washizu.

The dynamics of the Timoshenko beam were recast by Gopalakrishnan, Martin, and Doyle [11] so that the description only requires information at the end points. The resulting dynamic stiffness relations were assembled (akin to finite elements) allowing exact frequency dependent response for the Timoshenko beam irrespective of element length.

Using a boundary integral equation Tanaka and Bercin [26] developed the solution for the free vibration of a Timoshenko beam. A general Timonshenko beam of open cross-section with non-coincident shear centre and centroid was modelled. They showed that unacceptably large errors result from the simpler Bernoulli-Euler beam theory model (especially for higher order modes). Lee and Lin [18] developed an approximate solution for the transverse vibration of a non-uniform Bernoulli-Euler beam with time-dependent elastic boundary conditions.

The vibration characteristics of blades with multiple-load-paths (at the root) were determined by Lauzon and Murthy [17]. They developed a modified Galerkin's method to model a non-rotating beam undergoing coupled flapwise bending, chordwise bending,

---

[1]Timoshenko beam theory corrects for the rotary inertia and shear in classical beam theory [26].

twisting, and extensional motions. The derived natural frequencies of a simulated rotor compared well with both experimental results and a finite element approach.

A thorough survey and comparison of engineering beam theories for helicopter rotor blades was undertaken by Kunz [16]. The characteristics and differences amongst the various formulations were reviewed, and the results presented in a historical context.

D'Cruz [7] determined the location of forces on a plate. First the magnitude and location of a static point load on an infinite, and then semi-infinite, rectangular plate were determined. This procedure was then extended to harmonic point loads. These load magnitudes and locations were determined using arrays of discrete points on the plate. The solution involved the least-squares minimisation of an objective function, which was linear in the force magnitude. This load determination problem was found to be ill-conditioned near boundaries.

2   Equations Governing the Vibration of a Cantilever Beam

In this section we develop the PDE governing the transverse vibration of a beam.
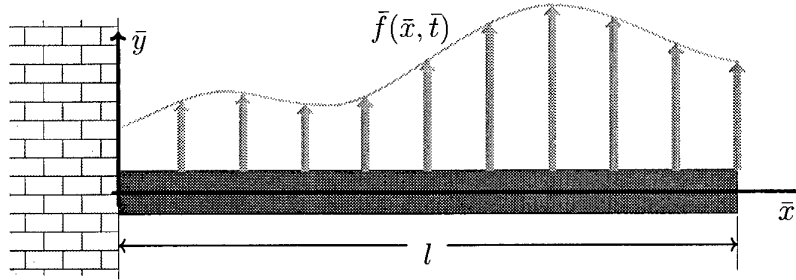

Figure 2.1: A cantilever beam with a non-uniform loading distribution $\bar{f}$, which varies with space and time. The beam has length l, mass per unit length m, and stiffness EI.

We begin by considering a cantilever beam of length l with load per unit length $\bar{f}(\bar{x}, \bar{t})$ that varies both spatially and temporally (see Figure 2.1). The spatial dimensions $\bar{x}$ and $\bar{y}$ define the distance along the beam and the beam's transverse deflection respectively. The temporal dimension is denoted by $\bar{t}$. Non-dimensionalising these quantities we obtain the non-dimensional variables

$$x = \frac{\bar{x}}{l}, \qquad\qquad y = \frac{\bar{y}}{l},$$

$$t = \bar{t}\sqrt{\frac{EI}{ml^4}}, \quad \text{and} \quad f = \frac{l^3}{EI}\bar{f},$$

where m, E, and I are the beam's mass per unit length, Young's modulus, and second moment of area (or cross-sectional area moment of inertia) respectively. For simplicity we assume the mass m and stiffness EI are constant along the beam.

3

We see from Figure 2.1 that the boundary conditions at the fixed end ($x = 0$) are

$$y(0, t) = 0 \qquad \text{and} \qquad \left.\frac{\partial y}{\partial x}\right|_{x=0} = 0. \qquad (2.1)$$

These two conditions, termed "geometric" boundary conditions, impose zero deflection and zero slope at the fixed end of the beam. Similarly we see that the free end has the boundary conditions

$$\left.\frac{\partial^2 y}{\partial x^2}\right|_{x=1} = 0 \qquad \text{and} \qquad \left.\frac{\partial^3 y}{\partial x^3}\right|_{x=1} = 0. \qquad (2.2)$$

These two conditions, termed "natural" boundary conditions, impose zero bending moment and zero shear at the free end of the beam. This last statement follows from the fact that (perpendicular to the beam) the bending moment and shear are respectively given by $EI\,\partial^2 y/\partial x^2$ and $EI\,\partial^3 y/\partial x^3$. For further details on the relation between bending moment or shear and derivatives of beam deflection see, for example, Young [30] or Timoshenko and Gere [27].

We denote the initial conditions as

$$y(x, 0) = y_0(x) \qquad \text{and} \qquad \left.\frac{\partial y}{\partial x}\right|_{t=0} = v_0(x), \qquad (2.3)$$

that is, y_0 and v_0 denote the initial deformation and velocity respectively.

Using Meirovitch [20, Eq. (5.43)] we know that the PDE governing the transverse vibration of a beam with constant mass and stiffness is given by

$$EI\frac{\partial^4 \bar{y}}{\partial \bar{x}^4} + m\frac{\partial^2 \bar{y}}{\partial \bar{t}^2} = \bar{f}(\bar{x}, \bar{t}), \qquad 0 < x < l,$$

or in non-dimensional variables

$$\frac{\partial^4 y}{\partial x^4} + \frac{\partial^2 y}{\partial t^2} = f(x, t), \qquad 0 < x < 1. \qquad (2.4)$$

The following assumptions were made in developing the PDE shown above:

- The rotation of the differential elements is insignificant (simple beam theory).
- The shear deformation is small in relation to the bending deformation (simple beam theory).
- The ratio between the beam's length and height is relatively large (say more than 10).
- The beam does not become too "wrinkled" in flexure.

Higher modes obtained by using Equation (2.4) are inaccurate because both the simple beam and the "wrinkling" assumptions are violated. One way to determine higher mode solutions would be to numerically solve the exact PDE governing beam vibration (that is, without the above assumptions).

3 Separation of Variables Solution

In this section we solve the PDE of a vibrating cantilever beam, developed in the previous section, using the separation of variables technique. For an explanation of this technique see, for example, O'Neil [21]. We follow a similar analysis by Meirovitch [20] (specifically pages 223–227 and 235–238), who determines the modal response of a hinged beam. (A hinged beam is one that has pin joints at either end and no joints along the beam.)

We assume the solution may be partitioned into a space dependent function $Y = Y(x)$ and a time dependent function $T = T(t)$, that is

$$y(x, t) = Y(x)T(t).$$

Substituting the above expression into the homogeneous form (that is, $f \equiv 0$) of the vibration PDE (Equation (2.4)) gives

$$Y^{(4)}T + Y\ddot{T} = 0,$$

and hence

$$\frac{Y^{(4)}}{Y} = -\frac{\ddot{T}}{T} = \beta^4,$$

where β is a constant from the separation of variables technique. The over-dot denotes differentiation with respect time (for example, $\ddot{T} = d^2T/dt^2$); while the dash and bracketed superscript denote differentiation with respect to space (for example, $Y'' = d^2Y/dx^2$ and $Y^{(4)} = d^4Y/dx^4$). The constant of separation β is related to the natural frequency of the dimensional beam $\beta^2\sqrt{EI/(ml^4)}$ (see, for example, Meirovitch [20, p. 226]).

The solution of the fourth order differential equation $Y^{(4)} - \beta^4 Y = 0$ is given by Tuma [28, p. 181] as

$$Y(x) = A\cosh(\beta x) + B\sinh(\beta x) + C\cos(\beta x) + D\sin(\beta x),$$

where A, B, C, and D are constants to be determined from the boundary conditions. Using the boundary conditions given by Equations (2.1) and (2.2) we have that

$$Y(0) = 0, \qquad\qquad Y'(0) = 0, \tag{3.1}$$

$$Y''(1) = 0, \quad\text{and}\quad Y^{(3)}(1) = 0.$$

Solving for the four constants using the above boundary conditions yields

$$Y_j(x) = A_j\left[(\cosh\beta_j x - \cos\beta_j x) - \alpha_j(\sinh\beta_j x - \sin\beta_j x)\right], \tag{3.2}$$

where β_j is the jth positive root of the equation

$$\cos\beta_j\cosh\beta_j = -1, \quad\text{and}\quad \alpha_j = \frac{\cosh\beta_j + \cos\beta_j}{\sinh\beta_j + \sin\beta_j} \tag{3.3}$$

is a constant, which we term the hyperbolic constant. In the above solution we have ignored all answers leading to the trivial solution $Y(x) \equiv 0$ (such as $A_j = 0$). Note that

all the solutions Y_j are orthogonal, that is, $\int_0^1 Y_i(x)Y_j(x)dx = 0$ if $i \neq j$. Kelly [14, p. 478] and Meirovitch [19, p. 163] give the same expression for the solution of a cantilever beam under free vibration as Equation (3.2).

We want to select A_j so that the solutions Y_n are not only orthogonal but are in fact orthonormal, that is,

$$\int_0^1 Y_i(x)Y_j(x)dx = \begin{cases} 0 & \text{if } i \neq j, \\ 1 & \text{if } i = j. \end{cases} \tag{3.4}$$

Using *Mathematica* [29] (a computer program that can perform symbolic manipulation) the constants A_j that satisfy this orthonormal condition were determined. Some tedious algebraic manipulation (using *Mathematica* and Abramowitz and Stegun [1]) then led to the solution

$$A_j{}^2 = \frac{\beta_j\left(\sinh\beta_j + \sin\beta_j\right)^2}{\beta_j\left(\sinh\beta_j + \sin\beta_j\right)^2 + 3\left(1 + \cos\beta_j\cosh\beta_j\right)\left(\cos\beta_j\sinh\beta_j - \cosh\beta_j\sin\beta_j\right)}.$$

Using the first part of Equation (3.3) the constants A_j simplify to

$$A_j = 1. \tag{3.5}$$

Thus Equation (3.2) becomes

$$Y_j(x) = \left(\cosh\beta_j x - \cos\beta_j x\right) - \alpha_j\left(\sinh\beta_j x - \sin\beta_j x\right). \tag{3.6}$$

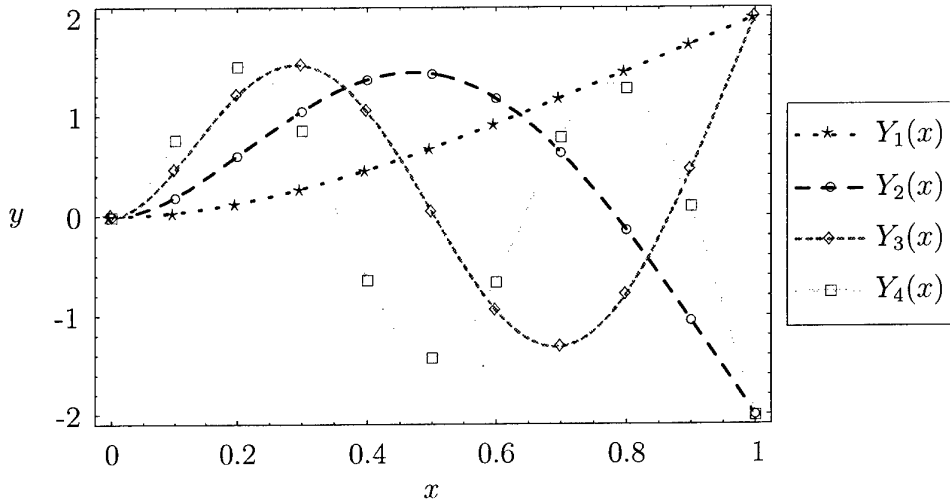The first four modes (using the above equation) are shown in Figure 3.1.

Figure 3.1: The first four vibration (or natural) modes of a cantilever beam (that is, $Y_j(x)$ for $j = 1, 2, 3, 4$).

Before concluding this section let's investigate the solutions of the equation governing the separation constant (the first part of Equation (3.3)). Re-arranging this equation gives

$$\cos\beta_j - \frac{1}{\cosh\beta_j} = 0,$$

and we now clearly see that for $\beta_j \gg 1$ this equation is well approximated by $\cos \beta_j = 0$.

Expanding the above displayed equation in a Taylor's series about $\beta_j = \pi(j - \frac{1}{2})$, ignoring all terms of $\mathcal{O}\left[\beta_j - \pi(j - \frac{1}{2})\right]^2$ and above, and solving for β_j yields the excellent approximation

$$\widehat{\beta}_j = \pi(j - \tfrac{1}{2}) + 2(-1)^j \mathrm{sech}\left[\pi(j - \tfrac{1}{2})\right] \tag{3.7}$$

$$\approx \pi(j - \tfrac{1}{2}) - 2(-1)^j \exp\left[-\pi(j - \tfrac{1}{2})\right] \tag{3.8}$$

$$\approx \pi(j - \tfrac{1}{2}), \tag{3.9}$$

where the hat notation "$\widehat{}$" denotes an approximation, that is, $\widehat{\beta}_j \approx \beta_j$.

The second approximation for the constant $\widehat{\beta}_j$ shown above comes from considering the hyperbolic function "sech" in exponential form. The symbols $\mathcal{O}$ defines the order, so for example if $f(x) = \mathcal{O}(x^2)$ then $|f(x)/x^2|$ is bounded.

Table 3.1 shows the accuracy of these three approximations for β_j to six significant figures. For each approximation both the value and relative error of the solution are shown, where the relative error is defined as $(\widehat{\beta}_j - \beta_j)/\beta_j$.

j	β_j	$\widehat{\beta}_j^*$	$|\beta_j - \widehat{\beta}_j^*|/\beta_j$	$\widehat{\beta}_j^\dagger$	$|\beta_j - \widehat{\beta}_j^\dagger|/\beta_j$	$\widehat{\beta}_j^\ddagger$	$|\beta_j - \widehat{\beta}_j^\ddagger|/\beta_j$
1	1.87510	1.96933	5.03×10^{-2}	1.98656	5.94×10^{-2}	1.57080	1.62×10^{-1}
2	4.69409	4.69442	7.09×10^{-5}	4.69440	7.06×10^{-5}	4.71239	3.90×10^{-3}
3	7.85476	7.85476	7.66×10^{-8}	7.85476	7.67×10^{-8}	7.85398	9.88×10^{-5}
4	10.9955	10.9955	1.02×10^{-10}	10.9955	1.02×10^{-10}	10.9956	3.05×10^{-6}
5	14.1372	14.1372	1.49×10^{-13}	14.1372	1.49×10^{-13}	14.1372	1.03×10^{-7}

Table 3.1: Values and errors of three approximations for the separation constant β_j. The superscripts "$*$", "$\dagger$", and "$\ddagger$" represent the approximations given by Equations (3.7), (3.8), and (3.9) respectively.

Using a similar approach for the constant α_j yields the excellent approximation

$$\widehat{\alpha}_j = \frac{1}{\tanh\left[\pi(j - \frac{1}{2})\right] - (-1)^j \mathrm{sech}\left[\pi(j - \frac{1}{2})\right]} + \frac{2(-1)^j \mathrm{sech}\left[\pi(j - \frac{1}{2})\right]}{\left\{(-1)^j + \sinh\left[\pi(j - \frac{1}{2})\right]\right\}^2} \tag{3.10}$$

$$\approx 1 + 2(-1)^j \exp\left[-\pi(j - \tfrac{1}{2})\right] \tag{3.11}$$

$$\approx 1. \tag{3.12}$$

In Equation (3.10) we have made use of the approximation for the separation constant β_j given by Equation (3.7). Table 3.2 shows the values and relative errors, $(\widehat{\alpha}_j - \alpha_j)/\alpha_j$, of these three approximations to six significant figures.

j	α_j	$\widehat{\alpha}_j^*$	$\lvert\alpha_j - \widehat{\alpha}_j^*\rvert/\alpha_j$	$\widehat{\alpha}_j^\dagger$	$\lvert\alpha_j - \widehat{\alpha}_j^\dagger\rvert/\alpha_j$	$\widehat{\alpha}_j^\ddagger$	$\lvert\alpha_j - \widehat{\alpha}_j^\ddagger\rvert/\alpha_j$
1	0.73410	0.68692	6.43×10^{-2}	0.58424	2.04×10^{-1}	1.00000	3.62×10^{-1}
2	1.01850	1.01850	5.76×10^{-6}	1.01800	4.92×10^{-4}	1.00000	1.81×10^{-2}
3	0.99922	0.99922	4.68×10^{-10}	0.99922	9.03×10^{-7}	1.00000	7.76×10^{-4}
4	1.00000	1.00000	3.77×10^{-14}	1.00000	1.69×10^{-9}	1.00000	3.36×10^{-5}
5	1.00000	1.00000	3.05×10^{-18}	1.00000	3.15×10^{-12}	1.00000	1.45×10^{-6}

Table 3.2: Values and errors of three approximations for the hyperbolic constant α_j. The superscripts "$*$", "$\dagger$", and "$\ddagger$" represent the approximations given by Equations (3.10), (3.11), and (3.12) respectively.

As can be seen from Tables 3.1 and 3.2 the approximations for the separation and hyperbolic constants are excellent (especially for $j > 2$).

4 Solution in terms of Different Loading Distributions

We now consider several different loading conditions. We will begin by looking at the simplest loading (impulse loading in § 4.1), then investigate the solution under a slightly more complex loading pattern (step loading in § 4.2). Finally, in § 4.3, we develop the solution in a more intrinsic way by making use of the beam's natural modes.

Let us consider the non-homogeneous solution to the vibrating beam problem. Using an approach analogous to Fourier series decomposition (or any orthogonal decomposition), we may represent the vibration solution as a series expansion of orthogonal functions. Using the homogeneous (and orthogonal) solutions given by Equation (3.6) we can write the vibration solution as

$$y(x,t) = \sum_{j=1}^{\infty} \psi_j(t) Y_j(x), \tag{4.1}$$

where ψ_j are the coefficients in the series expansion of the solution in terms of vibrational modes. We term the coefficients ψ_j the solution coefficients. Similarly the loading distribution has the series expansion

$$f(x,t) = \sum_{j=1}^{\infty} \phi_j(t) Y_j(x), \tag{4.2}$$

where $\phi_j(t)$ is the coefficient for the jth homogeneous solution. We term the coefficients ϕ_j the loading coefficients. Note that non-zero derivatives at the fixed end, that is

$$\left.\frac{\partial^i f}{\partial x^i}\right|_{x=0} \neq 0, \qquad \text{for } i = 0, 1, 2, \ldots,$$

are not efficiently represented by the formulation of Equation (4.2) (see Figure 3.1). In other words, even simple functions such as $\cos x$ would need a large number of modes to be well approximated.

If we substitute the vibration solution given by Equation (4.1) and the loading distribution given by Equation (4.2) into the PDE governing beam vibration (2.4) we have that

$$\sum_{j=1}^{\infty} \psi_j \, Y_j{}^{(4)} + \sum_{j=1}^{\infty} \ddot{\psi}_j \, Y_j = \sum_{j=1}^{\infty} \phi_j \, Y_j.$$

Since the fourth derivative of the jth mode is a multiple of the mode itself (that is, $Y_j{}^{(4)} = \beta_j^4 \, Y_j$), we have that

$$\sum_{j=1}^{\infty} Y_j \left(\ddot{\psi}_j + \beta_j^4 \, \psi_j - \phi_j \right) = 0.$$

The modes Y_j are orthogonal, however, so we must have that

$$\ddot{\psi}_j(t) + \beta_j^4 \, \psi_j(t) = \phi_j(t), \tag{4.3}$$

for all j. Solving this second order differential equation (DE) for the solution coefficients ψ_j determines the vibration response of the cantilever beam.

4.1 Non-Uniform Impulse Loading Along the Beam

Consider the discrete loading distribution shown in Figure 4.1. This loading configuration may be represented mathematically as a set of spatial-impulse loads, that is,

$$f(x,t) = \sum_{i=1}^{K} \delta(x - \xi_i) \, \Phi_i(t), \tag{4.4}$$

where Φ_i and ξ_i are the magnitude and location of the ith discrete load respectively, K is the number of discrete spatial-impulse loads, and $\delta(a)$ is the delta (or impulse) function defined by $\int_{a-\epsilon}^{a+\epsilon} \delta(x-a) f(x) dx = f(a)$ for any $\epsilon > 0$. Note that both the loadings Φ_i and locations ξ_i have been appropriately non-dimensionalised (see page 3), and that the load magnitudes Φ_i vary temporally. Figure 4.1 shows these new definitions superimposed on our cantilever beam. Finally, note that Equation (4.4) is composed of a set of impulse functions $\delta(x - \xi_i)$ only in space and not in time.

Multiplying both sides of Equation (4.2) by $Y_k(x)$ and integrating with respect to x over the length of the beam gives that

$$\int_0^1 \sum_{j=1}^{\infty} \phi_j(t) Y_j(x) Y_k(x) dx = \int_0^1 f(x,t) Y_k(x) dx,$$
.

where we have switched the left and right hand sides as compared to Equation (4.2). Assuming the series given by Equation (4.2) is "well behaved" we can change the order of
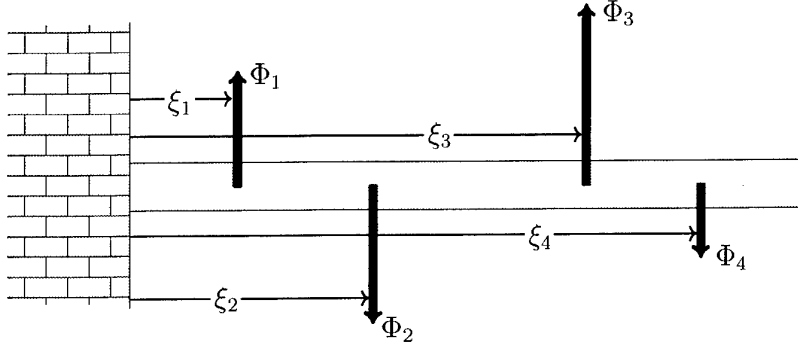
Figure 4.1: A cantilever beam with spatial-impulse loading Φ_i.

summation and integration. (For a more detailed discussion on the integration of series see Knopp [15, p. 341].) Furthermore, using Equation (4.4) in the right hand side yields

$$\sum_{j=1}^{\infty} \phi_j(t) \int_0^1 Y_j(x)Y_k(x)dx = \int_0^1 \sum_{i=1}^{K} \delta(x_i - \xi_i)\, \Phi_i(t)Y_k(x)dx$$

$$\sum_{j=1}^{\infty} \phi_j(t)\, \delta_{jk} = \sum_{i=1}^{K} \Phi_i(t) \int_0^1 \delta(x_i - \xi_i)\, Y_k(x)dx,$$

where δ_{jk} is the Kronecker delta function, and by definition $\delta_{kk} = 1$ and $\delta_{jk} = 0$ if $j \neq k$. In the left hand side of the above equations we have made use of the orthonormal property of the homogeneous solution (see Equation (3.4)) to get from the first line to the second line. We can change the order of integration and summation, on the right hand side, since both operations are finite. Using the definition of the delta generalised function we have that

$$\phi_k(t) = \sum_{i=1}^{K} \Phi_i(t)\, Y_k(\xi_i). \tag{4.5}$$

Thus our spatial-impulse loading (4.4) can be written as the sum of the beam's vibrational modes.

The analysis in the remainder of this subsection can be greatly simplified if we assume the loading is constant in time; we will later explain the need for this restriction. By "constant in time" we mean that the loading is applied as a step load, so that the loading is constant both before and after its application.

Under a constant temporal loading assumption, substituting Equation (4.5) into Equation (4.3), and solving for the resulting second order DE gives the solution

$$\psi_j(t) = \frac{1}{\beta_j^4} \sum_{i=1}^{K} \Phi_i\, Y_j(\xi_i) + \mathcal{A}_j \cos(\beta_j^2\, t) + \mathcal{B}_j \sin(\beta_j^2\, t),$$

where $\mathcal{A}_j$ and $\mathcal{B}_j$ are the constants from the solution of the DE.

Using the initial conditions $\psi_j(0) = 0$ and $\dot{\psi}_j(0) = 0$ (that is, zero initial deformation and velocity) we have that

$$\psi_j(t) = \frac{1}{\beta_j^4} \left[1 - \cos(\beta_j^2\, t) \right] \sum_{i=1}^{K} \Phi_i\, Y_j(\xi_i).$$

Hence the vertical deformation of a vibrating beam with zero initial conditions and spatial-impulse loading is given by

$$y(x,t) = \sum_{j=1}^{\infty} \frac{1}{\beta_j^4} \left[1 - \cos(\beta_j^2\, t) \right] \sum_{i=1}^{K} \Phi_i\, Y_j(\xi_i)\, Y_j(x). \tag{4.6}$$

We can now begin to see that having vibration information at one point on the beam (say from an accelerometer) would allow us to determine the loading distribution along the beam. To see this more clearly differentiate the solution given by Equation (4.6) twice with respect to time, which gives the acceleration of the beam as

$$\ddot{y}(x,t) = \sum_{i=1}^{K} \Phi_i \sum_{j=1}^{\infty} \cos(\beta_j^2\, t)\, Y_j(x)\, Y_j(\xi_i).$$

Changing the order of summation in the above expression may be technically incorrect (using classical definitions of convergence), since it is not at all clear that the series is convergent. In fact (using classical definitions of convergence) the series may prove to be divergent, since for j large we have that $Y_j(x) \approx \sin[\pi(j - \frac{1}{2})x] - \cos[\pi(j - \frac{1}{2})x]$. (For an interesting discussion on divergent series see Hardy [13], who states that depending on definitions some "classically" divergent series are in fact convergent.) As an aside note that this "non-convergence" result is not unexpected, remember that an impulse function excites all frequencies of a Fourier series equally. The fact that the impulse function is a *generalised function* (see for example Greenberg [12]) should alert us to these apparently unusual results.

If (for the sake of the argument) we assume the series to be convergent on physical considerations, then the above re-arrangement is permissible and the equation displayed above can be re-written in the form

$$\ddot{y}(x,t) = \sum_{i=1}^{K} \gamma_i(x,t)\Phi_i, \tag{4.7}$$

where

$$\gamma_i(x,t) = \sum_{j=1}^{\infty} \cos(\beta_j^2\, t)\, Y_j(x)\, Y_j(\xi_i).$$

An example will crystalise the idea of determining the magnitude of the loads Φ_i. Let's take K samples of acceleration, at times $t = t_1, t_2, \ldots, t_K$, from an accelerometer located at $x = \xi_*$ along the beam. As an example let $K = 3$, then from Equation (4.7) we have the linear system of K equations

$$\begin{bmatrix} \ddot{y}(\xi_*, t_1) \\ \ddot{y}(\xi_*, t_2) \\ \ddot{y}(\xi_*, t_3) \end{bmatrix} = \begin{bmatrix} \gamma_1(\xi_*, t_1) & \gamma_2(\xi_*, t_1) & \gamma_3(\xi_*, t_1) \\ \gamma_1(\xi_*, t_2) & \gamma_2(\xi_*, t_2) & \gamma_3(\xi_*, t_2) \\ \gamma_1(\xi_*, t_3) & \gamma_2(\xi_*, t_3) & \gamma_3(\xi_*, t_3) \end{bmatrix} \begin{bmatrix} \Phi_1 \\ \Phi_2 \\ \Phi_3 \end{bmatrix}.$$

Since the vector of accelerations on the left and the matrix of constants on the right are both known, the above linear system can easily be solved for the vector of unknown load magnitudes Φ_i on the right.

If the location of the applied loads were also unknown then Equation (4.7) would yield a non-linear system of equations in terms of Φ_i and ξ_i. As can be seen this non-linear system of equations would require $2K$ acceleration samples to solve for the magnitude and location of the unknown loads. Moreover, because the system is non-linear there is no guarantee that the solution would be unique.

Consider the following thought experiment. First uniformly space the loading locations along the beam, and let the number of these locations K tend to infinity. Secondly, using an accelerometer record the vibration at one point along the beam. We can then determine the loading distribution along the entire beam using vibration information from only one point on the beam! This thought experiment assumes we can record all frequencies (that is, an infinite number of natural frequencies). In reality we would be restricted by the bandwidth capability of our measuring system, which would in turn restrict the accuracy of our load reconstruction capability. Remember also that we have made the assumption that the beam doesn't become too "wrinkled", and hence we could not accurately model higher modes.

4.2   Non-Uniform Step Loading Along the Beam

Consider the discrete loading distribution shown in Figure 4.2. This loading configuration may be represented mathematically as a set of hat loads, that is,

$$f(x,t) = \sum_{i=0}^{K} h(x; \xi_i, \xi_{i+1}) \Phi_i(t), \qquad (4.8)$$

where $\xi_i < \xi_{i+1}$ for all $i = 0, 1, \ldots, K$, and

$$h(x; a, b) = \begin{cases} 0 & \text{if } x \leq a, \\ 1 & \text{if } a < x \leq b, \\ 0 & \text{if } x > b, \end{cases} \qquad (4.9)$$

is the hat function. The hat function loading representation given by Equation (4.8) uses the two spatial locations ξ_0 and ξ_{K+1}, which we define as $x = 0$ and $x = 1$ (the fixed and free ends) respectively. Again both the load magnitudes Φ_i and locations ξ_i have been appropriately non-dimensionalised.

Following a procedure that is analogous to the one used in the previous subsection we arrive at the solution for a hat loaded beam. For zero initial deformation and velocity ($y_0 = v_0 = 0$) the vertical deformation of a cantilever beam is given by

$$y(x,t) = \sum_{j=1}^{\infty} \frac{1}{\beta_j^4} \left[1 - \cos(\beta_j^2 t) \right] \sum_{i=0}^{K} \Phi_i \, \check{Y}_{ij} \, Y_j(x), \qquad (4.10)$$
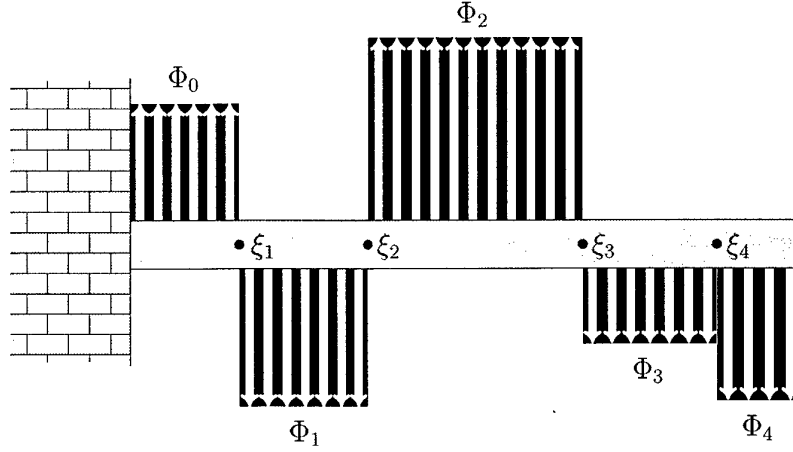
Figure 4.2: A cantilever beam with step loading Φ_i.

where

$$\breve{Y}_{ij} = \int_{\xi_i}^{\xi_{i+1}} Y_j(x)dx$$

$$= \frac{1}{\beta_j}\big[\,(\sinh\beta_j x - \sin\beta_j x) - \alpha_j\,(\cosh\beta_j x + \cos\beta_j x)\,\big]_{\xi_i}^{\xi_{i+1}}$$

is the integral of the jth natural mode over the ith beam segment.

4.3 Solution in Terms of Natural Modes

The problem of choosing beam segmentations ξ_i may be alleviated by deriving beam loading results in terms of the beam's natural frequencies. In this subsection we reconstruct the loading along a beam in terms of the beam's modes. (We will see that this type of construction leads to a more natural solution.) Figure 4.3 shows an example of this natural mode loading for the distribution $1.67Y_1(x) + 0.190Y_2(x) + 0.0889Y_3(x) + 0.390Y_4(x)$. The complete load is shown as the dark grey region, while the individual decomposed modes are shown as dashed lines.

In an analogous way to the previous two subsections we can express the loading coefficients ϕ_j in terms of the loading function $f(x,t)$. Multiplying both sides of Equation (4.2) by a natural mode and integrating over the length of the beam gives the jth loading coefficient as

$$\phi_j(t) = \int_0^1 f(x,t)Y_j(x)dx. \tag{4.11}$$

Assume the loading is periodic in time with period P, that is, $f(x, t + P) = f(x,t)$. The loading coefficient ϕ_j may then be expanded in a Fourier series

$$\phi_j(t) = a_{0j} + \sum_{i=1}^{\infty} [a_{ij}\cos(\omega_i t) + b_{ij}\sin(\omega_i t)], \tag{4.12}$$
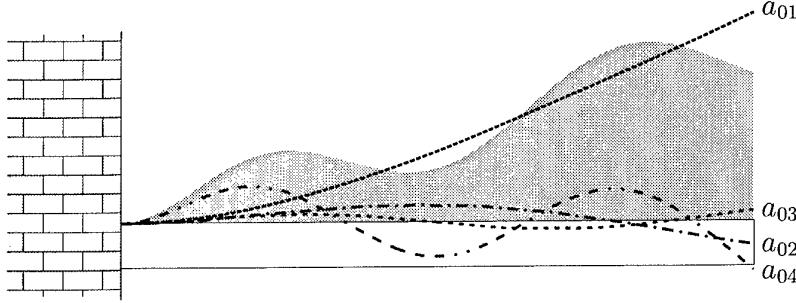
Figure 4.3: A cantilever beam with the loading decomposed into the beam's natural modes. The dashed lines represent the individual decomposed modes, while the dark grey region represent the sum of these modes (that is, the total loading).

where a_{ij} and b_{ij} are the Fourier coefficients for the cosine and sine expansions respectively and $\omega_i = (2\pi i)/P$ is the ith loading frequency.

The solution to the second order differential equation given by Equation (4.3) with the above equation substituted for the loading coefficient is given by

$$\psi_j(t) = \mathcal{A}_j \cos(\beta_j^2\, t) + \mathcal{B}_j \sin(\beta_j^2\, t) + \frac{a_{0j}}{\beta_j^4} + \sum_{i=1}^{\infty} \frac{a_{ij}\cos(\omega_i t) + b_{ij}\sin(\omega_i t)}{\left(\beta_j^4 - \omega_i^2\right)} \qquad (4.13)$$

(see, for example, Tuma [28, p. 180]).

Once again using the orthonormal property of the normal modes we have from Equation (4.1) that

$$\psi_j(t) = \int_0^1 y(x,t)Y_j(x)dx.$$

Hence for the initial condition $(t = 0)$ we have equating the above expression with Equation (4.13)

$$\mathcal{A}_j = \sigma_j - \frac{a_{0j}}{\beta_j^4} - \sum_{i=1}^{\infty} \frac{1}{\left(\beta_j^4 - \omega_i^2\right)}a_{ij} \qquad \text{and} \qquad \mathcal{B}_j = \frac{1}{\beta_j^2}\left[\tau_j - \sum_{i=1}^{\infty} \frac{\omega_i}{\left(\beta_j^4 - \omega_i^2\right)}b_{ij}\right],$$

where

$$\sigma_j = \int_0^1 y(x,0)Y_j(x)dx \qquad \text{and} \qquad \tau_j = \int_0^1 \dot{y}(x,0)Y_j(x)dx$$

are respectively the coefficients of the beam's initial *deformation* and *velocity* decomposed into the beam's natural modes. Substituting the above expressions for the constants $\mathcal{A}_j$ and $\mathcal{B}_j$ into Equation (4.13) gives the final form of the series expansion coefficients

$$\psi_j(t) = \left[\cos(\beta_j^2\, t)\right]\sigma_j + \left[\frac{1}{\beta_j^2}\sin(\beta_j^2\, t)\right]\tau_j + \left[\frac{1}{\beta_j^4}\left\{1 - \cos(\beta_j^2\, t)\right\}\right]a_{0j}$$
$$+ \sum_{i=1}^{\infty}\left\{\left[\frac{\cos(\omega_i t) - \cos(\beta_j^2 t)}{\left(\beta_j^4 - \omega_i^2\right)}\right]a_{ij} + \left[\frac{\sin(\omega_i t) - (\omega_i/\beta_j^2)\sin(\beta_j^2 t)}{\left(\beta_j^4 - \omega_i^2\right)}\right]b_{ij}\right\}. \qquad (4.14)$$

We want to determine how the accelerations at one location along the beam relate to the beam loading. Differentiate Equation (4.1) twice with respect to time to yields

$$\ddot{y}(x,t) = \sum_{j=1}^{\infty} \ddot{\psi}_j(t) Y_j(x),$$

which shows that the acceleration of the beam is related to the acceleration of the solution coefficients ψ_j. Differentiating Equation (4.14) twice with respect to time gives the acceleration of the solution coefficients as

$$\ddot{\psi}_j(t) = \left[-\beta_j^4 \cos(\beta_j^2 t) \right] \sigma_j + \left[-\beta_j^2 \sin(\beta_j^2 t) \right] \tau_j + \left[\cos(\beta_j^2 t) \right] a_{0j}$$

$$+ \sum_{i=1}^{\infty} \left\{ \left[\frac{\beta_j^4 \cos(\beta_j^2 t) - \omega_i^2 \cos(\omega_i t)}{\left(\beta_j^4 - \omega_i^2 \right)} \right] a_{ij} + \left[\frac{\omega_i \beta_j^2 \sin(\beta_j^2 t) - \omega_i^2 \sin(\omega_i t)}{\left(\beta_j^4 - \omega_i^2 \right)} \right] b_{ij} \right\}. \quad (4.15)$$

In the above expression all the quantities in square brackets are known. At first it would appear we can reconstruct the loading along the beam if we're given a set of acceleration measurements at one location on the beam. Unfortunately, the constant loading (that is, the coefficients a_{0j}) and the initial deformation (σ_j) are entangled, and using a single measurement location these unknowns cannot be disentangled.

The simplest way to see this entanglement between the initial deformation σ_j and the constant force a_{0j} is to apply two substitutions. Making the substitutions

$$\sigma_j + \Delta \sigma \qquad \text{and} \qquad a_{0j} + \beta_j^4 \Delta \sigma$$

for σ_j and a_{0j} respectively in Equation (4.15) and simplifying returns exactly the same expression (namely, Equation (4.15)) regardless of the value of $\Delta \sigma$. The fact that two different initial-deformation and temporally-constant-loading combinations give the same acceleration for the solution coefficient, means that these two unknowns (σ_j and a_{0j}) cannot be disentangled without additional information.

Would using strain instead of acceleration improve this entangled situation? Yes—but only mildly, since we have only gained one piece of additional information instead of the n pieces of information we require to approximate the loading using the first n modes.

We know that the strain is proportional to the bending moment, and hence strains are also proportional to $\partial^2 y / \partial x^2$. (The constant of proportionality between strain and this second derivative is the distance, measured in the bending plane, from the beam's neutral axis to the desired strain location.) Differentiating Equation (4.1) twice with respect to the horizontal distance along the beam we have that

$$\frac{\partial^2 y}{\partial x^2} = \sum_{j=1}^{\infty} \psi_j(t) Y_j''(x), \qquad (4.16)$$

and from Equation (3.6) the second derivative of the jth natural mode is

$$Y_j''(x) = \beta_j^2 \left\{ \left[\cosh\left(\beta_j x\right) - \cos\left(\beta_j x\right) \right] - \alpha_j \left[\sinh\left(\beta_j x\right) - \sin\left(\beta_j x\right) \right] \right\}.$$

If we use strain instead of acceleration to determine the loading, then we would use the solution coefficients themselves (Equation (4.14)) instead of their accelerations (Equation (4.15)). As already mentioned above, using strain instead of acceleration improves the situation slightly (it gives us one additional piece of information). To see that the initial deformation and temporally-constant force are still entangled we will again use substitutions, but this time use multiple modes instead of just one. Making the substitutions

$$\sigma_1 + \Delta\sigma, \qquad a_{01} + \beta_1^4 \Delta\sigma, \qquad \sigma_j - \frac{Y_1''(\xi_*)}{Y_j''(\xi_*)}\Delta\sigma, \qquad \text{and} \qquad a_{0j} - \frac{Y_1''(\xi_*)}{Y_j''(\xi_*)}\beta_j^4 \Delta\sigma$$

for σ_1, a_{01}, σ_j, and a_{0j} (for $j \geq 2$) respectively in Equation (4.16) and simplifying returns exactly the same expression (namely, Equation (4.16)) regardless of the value of $\Delta\sigma$. As defined earlier, the spatial position ξ_* represents the location of the measurement device (in this case a strain gauge).

Near the fixed end of the beam, from an implementation point of view, strain measurements would be preferable to acceleration measurements, since strains would tend to be high in this region while accelerations would be low.[2]

In a similar way we can show that the Fourier coefficients a_{ij} and b_{ij} are entangled with the initial deformation coefficient σ_j and initial velocity coefficient τ_j respectively.

In summary, we have shown that using acceleration or strain at one location alone is not enough to simultaneously determine the initial conditions and loading distribution. In fact, we cannot determine loading distributions that vary with time—even if we know the initial conditions. We can, however, determine the temporally-constant loading distribution along the beam provided we know the initial deformation (note that we do *not* require the initial velocity to determine this loading distribution).

5   Simulation

In this section we report on a simulation of load prediction on a simple cantilever beam. The transient response of a finite element (FE) cantilever model is used to determine the beam's strain at one location. To test the load prediction technique developed in § 4.3, we predict the load distribution given the transient strain response at one location along the FE model.

The beam arbitrarily chosen to verify this load prediction capability was a tube 1000 mm in length, with a wall thickness of 10 mm and a square cross-section of 50 mm by 50 mm (outer dimensions). The Young's modulus and density of this tube were 72.40×10^9 N/m^2 and 2.768×10^3 kg/m^3 respectively. (The Poisson's ratio and the shear modulus were 0.3 and 27.94×10^9 N/m^2 respectively. However, these two properties were not necessary for the vibration response solution.) The constant load $x^2(1-x)$ was applied as a step function, where x is the distance (in metres) along the tube from the fixed end. This load represents a cubic distribution with zero load at both ends and zero slope at the fixed end of the tube. This step load was instantaneously applied at $t = 0$,

---

[2]Thanks to Shane Dunn (a colleague at AMRL) for making me aware of this point.

that is, the load may be represented as

$$x^2(1 - x)\, h(t, 0, \infty),\tag{5.1}$$

where $h(t, 0, \infty)$ is the hat function defined in Equation (4.9).

For simplicity we set the initial conditions to zero, that is, the beam initially had zero deformation and zero velocity.

We will first describe how we derived the so called "exact" solution for this verification problem in § 5.1. We then describe how the FE solution was obtained in § 5.2. Finally, we describe how successful the load prediction technique was, and also discuss some practical problems in § 5.3.

5.1   The Exact Solution

The exact solution of a cantilever beam's response to the step load given by Equation (5.1) was found using the solution procedures developed in § 4.3. The magnitudes of the first twenty load coefficients (a_{0j} in Equation (4.12)) of the exact solution are shown in Figure 5.1.
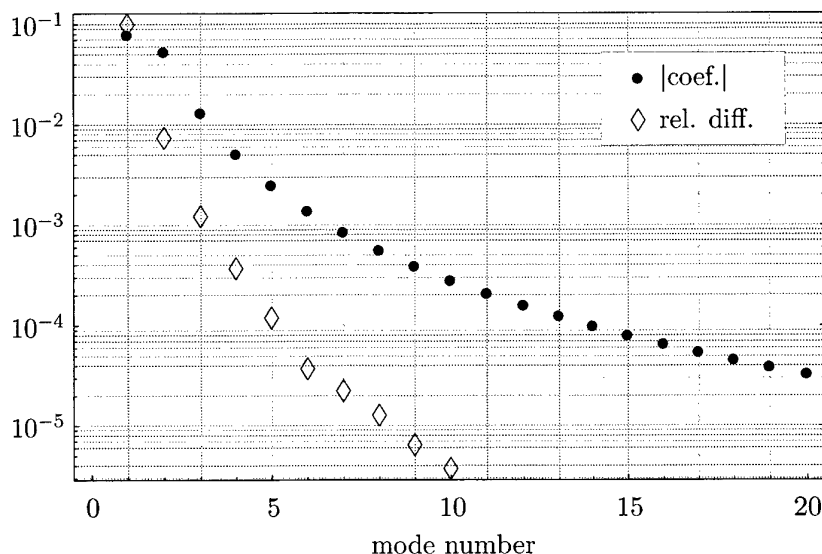

Figure 5.1: The magnitude of the exact solution's coefficients (denoted by •) plotted against the mode number. The relative difference (denoted by ◇) between using the corresponding number of modes as compared to the 20 mode solution.

These load coefficients were calculated using one-hundred digit arithmetics. This high accuracy was required because of the precision loss for the higher order modes was significant. For example, in calculating the load coefficient for the twentieth mode at least 26 digits of accuracy were lost. The loss of accuracy is due to the subtraction of numbers

with almost identical values, which we see when we re-write Equation (3.6) (the expression for the beam modes) as

$$Y_j(x) = (1 - \alpha_j) \sinh \beta_j x + (\sin \beta_j x - \cos \beta_j x) + \left[e^{-\beta_j x} - (1 - \alpha_j) \sin \beta_j x \right].$$

Despite the fact that $(1 - \alpha_j) \approx 2(-1)^{j+1} e^{-\pi(j-1/2)}$, see Equation (3.11), the first term in the above equation is not necessarily small for j large. For example, setting $x = 1$ and using the approximations given by Equations (3.9) and (3.11) gives the approximation $(1 - \alpha_j) \sinh \beta_j x \approx (-1)^{j+1} [1 - e^{-\pi(2j-1)}]$, which is of order unity for j large. This sort of cancellation leads to the large accuracy losses in calculations involving higher modes.

Also shown in the log-linear plot of Figure 5.1 is the relative difference between using only the first n modes as compared to using the first twenty modes. This relative difference was calculated as

$$\text{relative difference} = \frac{\sqrt{\dfrac{1}{t_{\text{fin}} + 1} \displaystyle\sum_{t_i=0}^{t_{\text{fin}}} \left[y_{20}(\xi_*, t_i \, \Delta t) - y_n(\xi_*, t) \right]^2}}{\sqrt{\dfrac{1}{t_{\text{fin}} + 1} \displaystyle\sum_{t_i=0}^{t_{\text{fin}}} \left[y_{20}(\xi_*, t_i \, \Delta t) \right]^2}}, \qquad (5.2)$$

where t_{fin} is the number of temporal samples taken for the evaluation of the relative error $y_{20}(x, t)$, and $y_n(x, t)$ are the solutions with 20 modes and n modes respectively, and Δt is the time step between temporal samples. (In our case $t_{\text{fin}} = 1600$ and the non-dimensional time step was $\Delta t = \sqrt{EI/(ml^4)}/1600$, see § 5.2 for an explanation of these value.) The relative difference defined by Equation (5.2) is merely the standard deviation of the difference between the twenty mode and the n mode solutions, relative to the standard deviation of the twenty mode solution. (This measure can also be thought of as a root mean squared or 2-norm measure.) In Figure 5.1 the relative difference of using fewer than twenty modes was plotted only up to ten modes, which was the number of modes used in the exact solution. In other words, in the following sections what we term the "exact" solution contains only the first ten modes.

5.2 The Finite Element (FE) Solution

The FE package "Nastran" was used to solve for the vibration response of our square tubular beam.[3] The final FE model used 1600 beam elements (of type "Bar2"), and the beam's response was calculated with time steps of 1/1600th of a second. The FE model was fixed both from moving in translation and rotation at one end of the beam, and was free to move at the other end.

The loading was applied as point loads at the nodes joining the beam elements, and hence the actual loading distribution along the beam can be represented by a sum of spatial-impulse loads. In other words, the load may be written as

$$\sum_{i=0}^{K} x^2 (1 - x) \, \delta(x - \xi_i)/K,$$

---

[3]Thanks to Soon-Aik Gan (a colleague at AMRL) for developing the Nastran model.

where ξ_i is the distance (in metres) from the fixed end to the ith node and $K+1$ is the number of nodes ($K = 1600$ in our case). The factor of $1/K$ is required in this load distribution so that the overall force on the beam is the same as its continuous counterpart $\int_0^1 x^2(1-x)dx$. By integrating the above node loading over the beam we see that the error in the discretised node loading is $1/(12K^2)$, and hence for our 1600 element FE model the total load on the beam has a relative error of 3.5×10^{-7}.

The final time step and number of elements were decided upon after comparing several solutions with varying time steps and beam elements. The relative differences between the solution with 1600 beam elements (and 1600 time steps) and several other solutions are shown in Table 5.1. These relative differences were calculated as the standard deviation of the difference divided by the standard deviation of the 1600 element solution, see Equation (5.2).

NUMBER OF ELEMENTS	100	200	400	800
TIME STEPS (SEC)	1/100	1/200	1/400	1/800
RELATIVE DIFFERENCE	9.4×10^{-4}	9.3×10^{-4}	2.3×10^{-4}	2.9×10^{-5}

Table 5.1: The relative difference between several different FE solutions, as compared to the FE solution with 1600 elements and a time step of 1/1600th of a second.

In order to simulate data from a strain gauge, the stress on the upper side of the beam, 50 mm along the horizontal from the fixed end, was extracted from the FE results. The stress was then scaled to the non-dimensional strain result given by the exact solution. Figure 5.2 shows, at $x = 0.05$, the strain response to the applied load. The exact solution is shown as the thick black line, while the FE solution is shown as the thick grey line. The difference between these two solutions—that is, the error in the FE solution—is shown as the thin black line.

As was expected, the FE solution diverges more from the exact solution as time progresses. The initial cycles (up to approximately 1.8 non-dimensional time units) has a comparatively small error, and hence we use this portion of the transient strain response to predict the load on the FE beam. Incidently the period of this first cycle is approximately the period of the first mode, which demonstrates the dominance of the first mode.

5.3 Simulation Results of Load Prediction

The results are mainly shown in two forms: (i) plots of the predicted load coefficients versus mode number and (ii) comparison plots of the predicted load and applied load along the beam.

The load coefficients (that is, the a_{0j} in Equation (4.12)) were determined using the technique developed in § 4.3 and the strains derived from the transient FE solution. To reduce the error introduced by the discretisation within the FE package Nastran (see
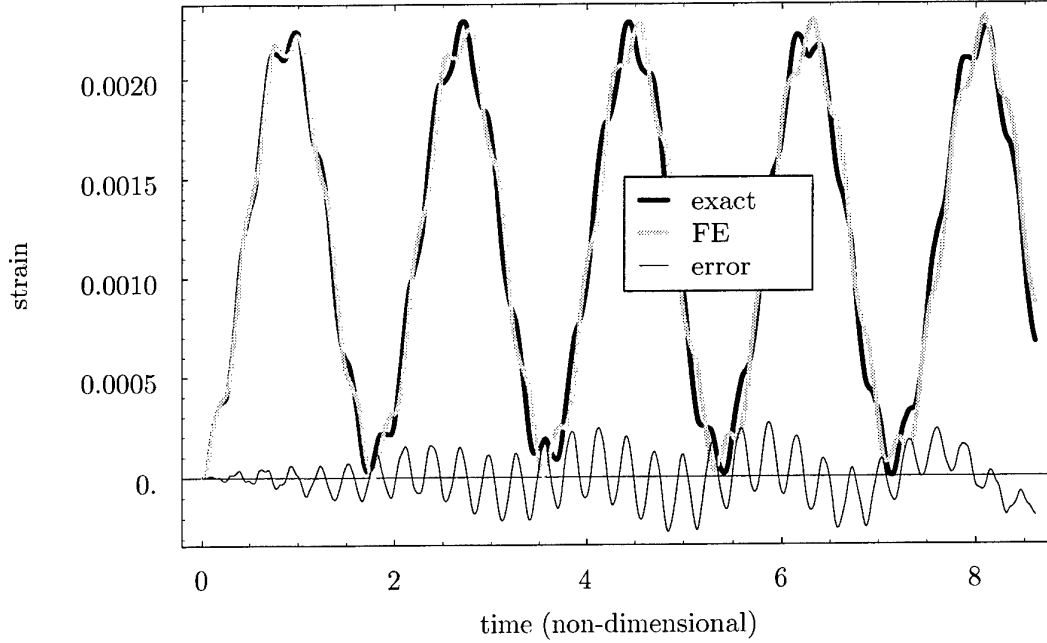
Figure 5.2: The strain response at x = 0.05 to a constant load $x^2(1-x)$ applied as a step function at time t = 0. The exact and FE solutions are shown as the thick black and thick grey lines respectively, while the error in the FE solution is shown as a thin black line.

Figure 5.2), the simulated strain measurements were taken exclusively from within the first period (that is, $t \lesssim 1.8$).

Figure 5.3 shows a comparison between the predicted and the exact load coefficients. As can be seen, the error is larger in the higher modes than the lower modes. The first forty-nine simulated strain measurements were used to determine the load coefficients shown in Figure 5.3. This number of strain measurements was chosen because it minimised the prediction error. We will see later that the number of strain measurements used to predict the load coefficient has a strong effect on the resulting prediction error.

Trying to predict the first ten load coefficients with forty-nine strain measurement resulted in an over-determined system of equations. We solved this over-determined system using singular value decomposition, which is equivalent to using least squares (see, for example, Golub and van Loan [10, p. 242]).

Figure 5.4 shows a plot of the predicted load distribution on the FE beam model. Notice the relatively high frequency oscillation of the predicted load (broken grey line) about the exact solution (solid black line). This oscillation is predicted by the larger errors of the higher modes shown in Figure 5.3.

In order to measure how well our load prediction technique works, we define a normalised error in terms of the coefficients of the load's modes

$$\text{normalised error} = \sqrt{\frac{\frac{1}{N}\sum_{j=1}^{N}\left(a_{0j} - \widehat{a}_{0j}\right)^2}{\frac{1}{N}\sum_{j=1}^{N}\left(a_{0j}\right)^2}}, \tag{5.3}$$
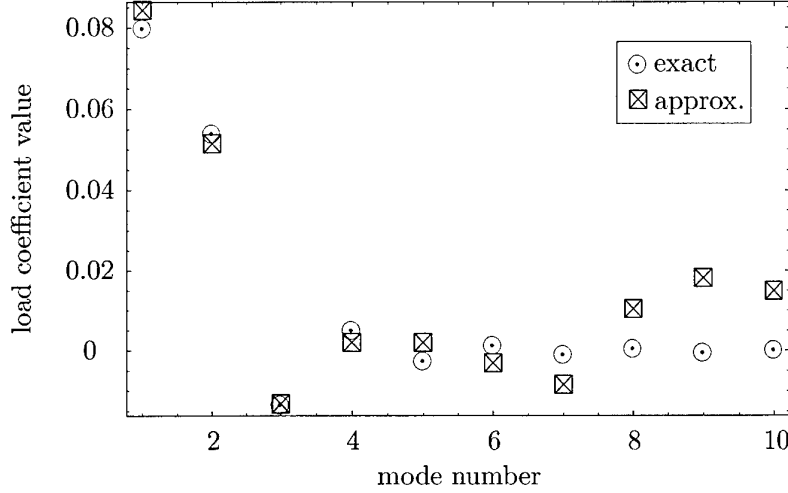
Figure 5.3: Comparison of the exact load coefficients (denoted by ⊙) and the predicted load coefficients from the FE derived strains (denoted by ⊠).

where N is the number of modes in our exact solution (for us $N = 10$), a_{0j} are the coefficients of the exact solution's load modes (see Equation (4.12)), and $\widehat{a}_{0j}$ are our predictions of a_{0j}. The summation in the numerator goes up to N, so if we are only predicting the first n modes of the load (in Figure 5.5, for example, n is either three, six, or nine), then $\widehat{a}_{0j} = 0$ for $j = n+1, n+2, \ldots, N$.

The definition of normalised error given in Equation (5.3) is in fact closely related to the error in terms of absolute areas. This statement shouldn't come as a surprise given that the form of this normalised error resembles Parseval's identity for the Fourier series (see, for example, Spiegel [25]). In other words, the normalised error is approximately equal to the area between the predicted and exact load distributions divided by the area under the exact load distribution (refer to Figure 5.4).

We now justify the above statement. Substituting Equation (4.2) for the load distribution we have that

$$\int_0^1 [f(x,t)]^2 \, dx \approx \int_0^1 \left[\sum_{j=1}^N \phi_j(t) Y_j(x) \right]^2 dx$$

$$= \int_0^1 \left[\sum_{j=1}^N \phi_j^2(t) Y_j{}^2(x) + 2 \sum_{j=1}^{N-1} \sum_{k=j+1}^N \phi_j(t)\phi_k(t) Y_j(x) Y_k(x) \right] dx$$

$$= \sum_{j=1}^N \phi_j^2(t) \int_0^1 Y_j{}^2(x) dx + 2 \sum_{j=1}^{N-1} \sum_{k=j+1}^N \phi_j(t)\phi_k(t) \int_0^1 Y_j(x) Y_k(x) dx$$

$$= \sum_{j=1}^N \phi_j^2(t), \tag{5.4}$$

where we have made use of Equation (3.4) (that is, the orthonormality of the beam modes)
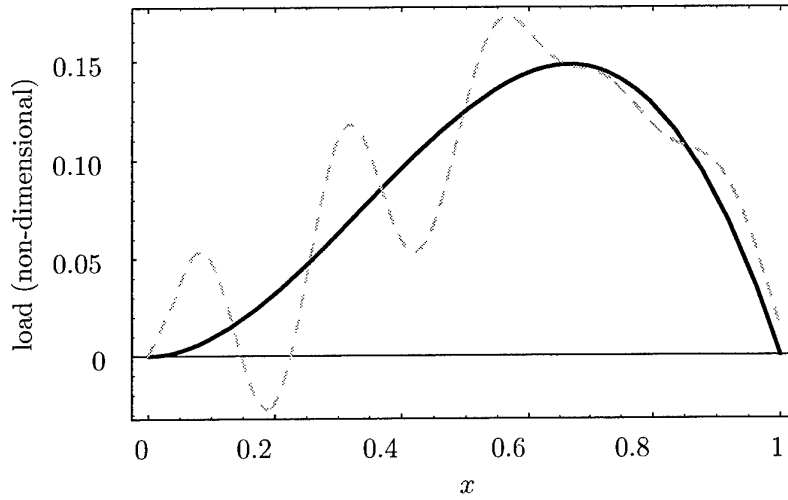
Figure 5.4: Plot of predicted load distribution using the transient strain response of the FE model. The load applied to the FE model is shown as the solid black line, while the predicted load is shown as a broken grey line. The horizontal axis is the non-dimensional distance from the fixed end of the beam.

in going from the second last line to the last line. In the first line of the above expressions the left and right hand sides are approximately equal, instead of exactly equal, because the number of modes in the "exact" solution is finite. Using Equation (5.4) and Hölder's inequality for integrals (see, for example, Spiegel [25]) we have that

$$\int_0^1 |f(x,t)| \, dx \leq \left\{ \int_0^1 [f(x,t)]^2 \, dx \right\}^{1/2}$$
$$\approx \sqrt{\sum_{j=1}^N \phi_j^2(t)}.$$

The above inequality shows the relation between the area under the load and the coefficients of the load's modes.

As we've already noted the error in predicting the load was sensitive to the number of strain measurements used. In addition, the load prediction error was also sensitive to the number of load modes we were trying to predict. Figure 5.5 shows how error varies with these two parameters. The black, dark grey, and light grey lines represent the load prediction of the first three, the first six, and the first nine modes respectively. The horizontal axis shows the number of strain measurements used to predict the load, while the vertical axis shows the normalised error of the resulting prediction.

In order to use Figure 5.5 to determine how well our prediction technique works, we need to know the quality of the FE results from which we are deriving the measured strains. The relative error in the FE solution's strain response was calculated as: the root mean square (RMS) of the difference between the exact and FE solution divided by the RMS of the exact solution. For the first fifty strain measurements, the normalised error in the FE
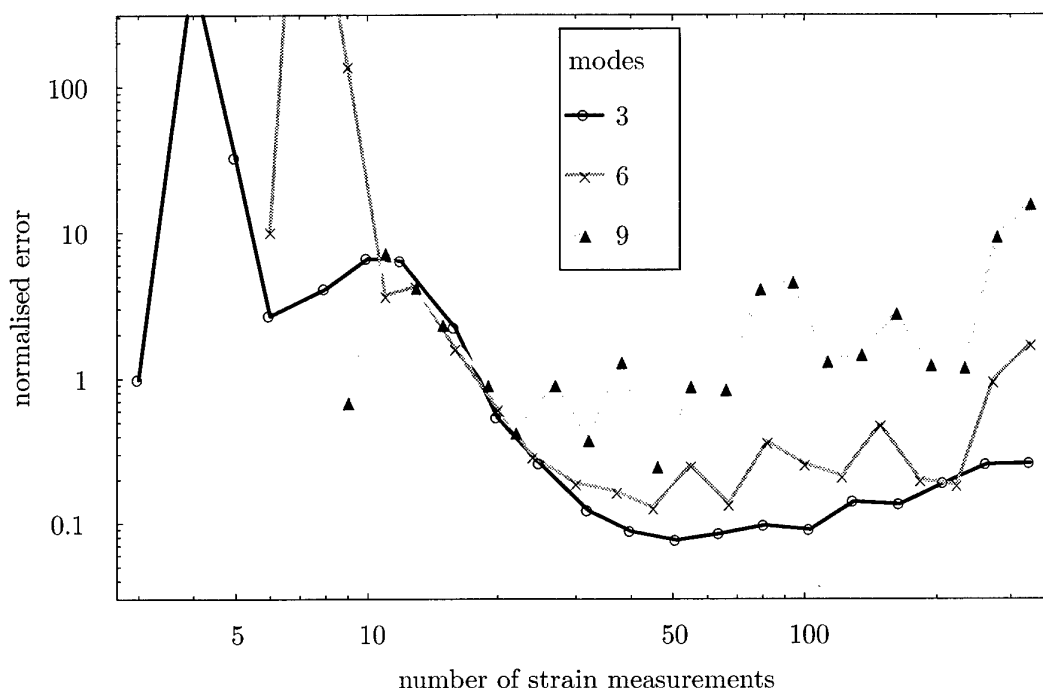
Figure 5.5: *The normalised error of the load prediction (vertical axis) for several different configurations. The horizontal axis shows the number of strain measurements used to predict the load. The number of modes used to predict the load varied from three* o, *through six* ×, *to nine* ▲ *modes.*

response was approximately 0.03, that is, about 3% error. From Figure 5.5, we see that only the first three modes could be predicted to within about 10% error, which is larger than the error in the measurements. The error in predicting a high number of modes, nine for example, resulted in excessively large errors (as shown in Figure 5.4, which was a prediction example with the least possible error). These preliminary results suggest that the load prediction technique is sensitive to noise, and as we show below, this is indeed the case for higher mode predictions.

Before leaving Figure 5.5, note the strong relation between the error and the number of strain measurements used to predict the load. In most cases, the optimal solution is an order of magnitude more accurate than most other solutions (in fact, several orders of magnitude better than an ill chosen number of measurements). We also see that the error, after an initial jump, starts decreasing to its optimal value, after which time the error rises with the number of measurements used in the prediction. We can easily explain the rise in errors with increasing measurements by referring back to Figure 5.2, where we see that the errors in the FE solution rise with increasing time.

Without knowing the exact solution *a priori* it's hard to determine the optimal number of measurements to use in load prediction. As we see from Figure 5.5 if we choose too few measurements the results could be meaningless, while choosing too many measurements leads us away from the optimal solution. Although it's better to choose too many

measurements than too few, it's best to get it right. One way to achieve a near optimal solution would be to plot the RMS of the difference between successive predictions of load coefficients versus the number of measurements used for the prediction. We should see a minimum near the optimal solution. In other words, the coefficients are relatively stable near the optimal solution (see the error of the three mode solution in Figure 5.5). A plot of RMS difference between successive solutions would also alert the user to unstable solutions, which are probably erroneous (for example see the errors of the nine mode solutions in Figure 5.5).

We now return to the issue of load prediction sensitivity to noise. In order to determine the effects of noise on load prediction, we will add 1% random white noise to the exact strain response. We will then predict the load distribution of this contaminated signal.

Figure 5.6 shows what happens when we try to predict the higher load modes of the exact strain response with 1% white noise added. Figure 5.7 shows the predicted load response. As can be seen from these plots it only takes a small amount of error to destroy the higher mode signal. Twenty-five strain measurements were used to derive the load prediction results shown in Figure 5.6 and 5.7; this number of measurements resulted in the best possible approximation. Using either more or fewer strain measurements led to load prediction results with significantly larger errors.
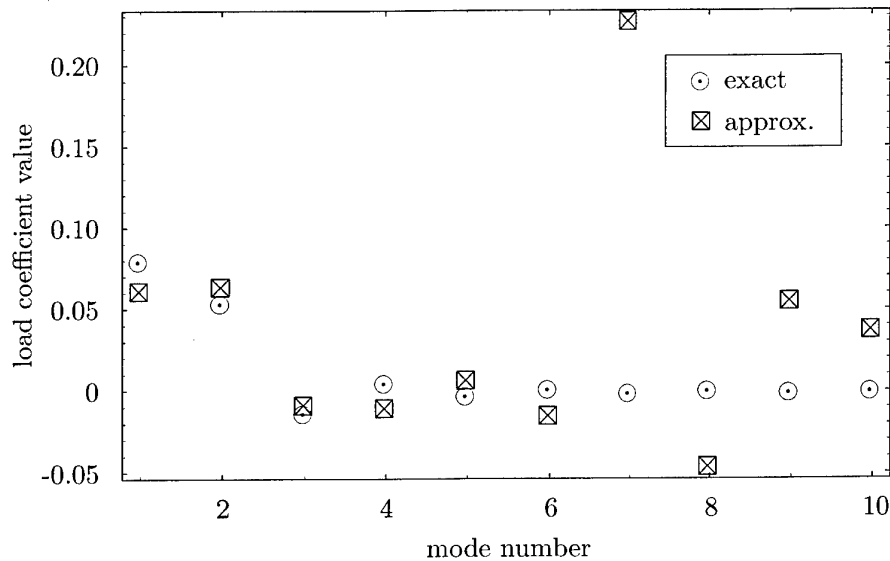

Figure 5.6: Comparison of the exact load coefficients (denoted by ⊙) and the predicted load coefficients for the exact strain response with 1% white noise added (denoted by ⊠).

In contrast, the low mode signals are quite robust as illustrated in Figure 5.8, which shows the prediction of only the lower load modes. Forty-five strain measurements were used to derive the load prediction results shown in Figure 5.8, which resulted in a load prediction with the lowest error. Due to the stability of the solution, choosing a larger
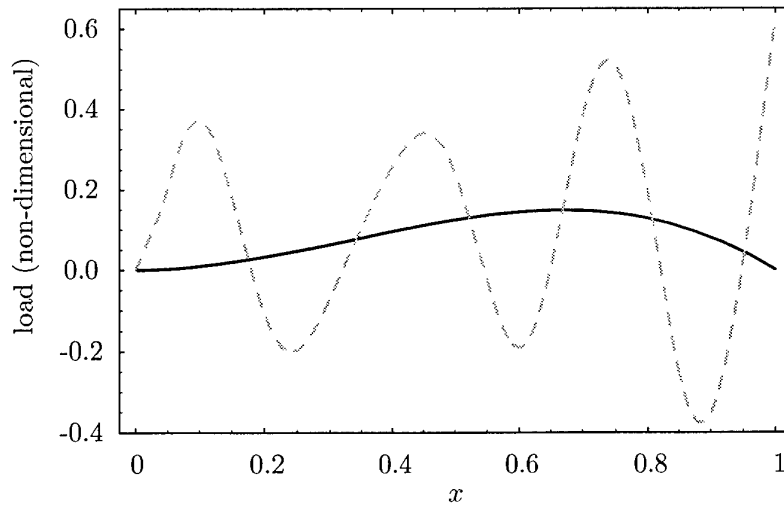
Figure 5.7: Plot of predicted load distribution along the beam using the transient exact strain response with 1% white noise added. The exact applied load is shown as the solid black line, while the predicted load is shown as a broken grey line. The horizontal axis is the non-dimensional distance from the fixed end of the beam.

number of strain measurements led to only marginally poorer load predictions.
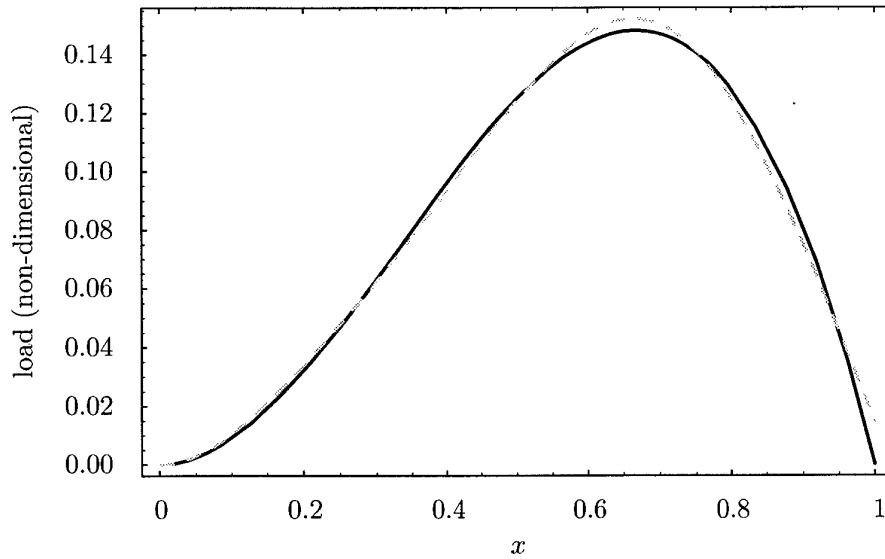

Figure 5.8: Plot of predicted load distribution (lower modes only) using the transient exact strain response with 1% white noise added. The exact applied load is shown as the solid black line, while the predicted load is shown as a broken grey line. The horizontal axis is the non-dimensional distance from the fixed end of the beam.

6 Discussion

Let us now consider the assumptions we have made; we will order these assumptions from most restrictive to least restrictive. Future directions for load determination are then outlined.

The most restrictive assumption (in fact a requirement) is that we know the initial deformation to determine the loading distribution (which is constant in time). (We later show how to overcome the restriction of a loading distribution that is constant in time.) In reality, for continuous monitoring of rotor blades we would not have this information. As such this requirement of knowing the initial deformation places a severe restriction on using this approach to determine the rotor blade loading distribution.

The second most restrictive assumption (which was an implicit one) is the form of the PDE governing vibration in the beam. The implicit assumption made in using the PDE given by Equation (2.4) is that the beam's vibration is not damped. In reality, we would expect the aerodynamic damping to play some role, and this may cause coupling between the modes.

Likewise we have ignored chordwise effects without knowing their influence (if any). Quite clearly if the rotor blades twist, then the stiffness properties would change resulting in a different vibration response (stiffness variation is further discussed below).

The formulation we have undertaken has assumed that all natural frequencies (an infinite number of them) are measured. In reality all the infinite summations developed in this report would be truncated to finite summations, which would lead to an aliasing effect. We stated earlier (see page 5) that the natural frequencies of a cantilever beam are given by $\beta^2\sqrt{EI/(ml^4)}$. Using Equation (3.9) we then have that the natural frequencies are

$$\pi^2(j - \tfrac{1}{2})^2\sqrt{\frac{EI}{ml^4}} + \mathcal{O}\left(e^{-\pi j}\right).$$

That is, the natural frequencies go up quadratically with mode number, and hence it becomes increasingly harder to capture higher natural frequencies. We would expect that the high frequency modes would have small amplitudes, and so the aliasing effects would be of second order as compared to the low frequency mode amplitudes. This expectation was borne out by the simulations in § 5.

The location of the accelerometer would also be crucial under some circumstances. It would be imprudent to place the accelerometer at one of the lower mode's stationary nodes. For example, placing the accelerometer at $x \approx 0.358$ would almost certainly reduce, if not completely eliminate, the vibration signal from the fourth mode (see Figure 3.1). Fortunately, only the higher modes of a cantilever beam have nodes near the fixed end. For example, placing the accelerometer at $x \approx 0.05$ (that is, 5% along the beam from the fixed end) would only affect modes equal to or higher than the twenty-fifth mode. In general, higher modes will have their first stationary node at $x \approx 5/(4j - 2)$, where j is the mode number. This approximation, of the first root of the jth mode, comes from Equation (3.6) and makes use of the relation $\cosh\theta - \sinh\theta = e^{-\theta}$ and the approximations given by Equations (3.9) and (3.12).

Using the same principles, we can extend this load determination technique (using

vibration at a single point) to non-constant mass and stiffness problems. However, we would then be forced to solve the governing PDE numerically, which would add an extra degree of difficulty. We have already mentioned that a twisting blade would have varying stiffness. Similarly centrifugal effects would add considerable stiffness to a rotor blade; that is, different rotational speeds would produce different blade stiffnesses. The differential equation (DE) governing the vibration response of a beam subject to an axial load F is given by Kelly [14, p. 502] as

$$EI\frac{\partial^4 \bar{y}}{\partial \bar{x}^4} - F\frac{\partial^2 \bar{y}}{\partial \bar{x}^2} + m\frac{\partial^2 \bar{y}}{\partial \bar{t}^2} = \bar{f}(\bar{x}, \bar{t}).$$

Notice the only difference between the above equation and the DE we used (Equation (2.4)) is the term $F\partial^2 \bar{y}/\partial \bar{x}^2$. The above expression is derived by Meirovitch [19, p. 440–3] from first principles.

We have only briefly touched on the effects of noise, especially the sensitivity of the solution with respect to noise. Intuitively we would expect that noise would only be a problem for higher frequency modes (namely the modes we have truncated), and so noise may not be a cause for concern. However, the results shown in Figure 5.6 (and associated simulations of § 5) cast doubt on this intuition.

On a helicopter we probably couldn't easily attach an accelerometer or a strain gauge to a rotor blade, and hence would have to place it on some adjacent structure. This adjacent structure may be subject to damping and vibration itself, which may act as noise on the rotor blade's vibration signal. A similar but more severe problem would arise from the vibration of the non-measured rotor blades. All the blades would have almost identical vibration responses, and hence it would be hard (if not impossible) to distinguish the vibration signal from the desired blade (especially if measurements were undertaken on some adjacent structure).

In § 4.3 (the most promising approach) we assume the loading could be decomposed into the shape of the natural modes (see Equation (4.11)). From the boundary conditions (Equations (3.1)) and Figure 3.1 we see that all the natural modes have both zero deformation and zero slope at the fixed end of the beam ($x = 0$). Hence we cannot model a non-zero load at the fixed end. In fact, non-zero loads close to the fixed end will necessarily involve high frequency mode shapes in their representation (due to the Gibbs phenomenon).

Superficially, the assumption of temporally-constant loading distribution appears very severe. However, there is nothing to stop us partitioning the rotation of a helicopter blade into several time segments, and considering the loading constant over each of these segments. Given that the rotation frequency of the main rotor on helicopters is relatively low (4.3 Hz for the Black Hawk) as compared to strain recording capabilities, we could easily carry out this segmentation approach to reconstruct a temporally-varying loading distribution. Figure 6.1 shows an example of how we can approximate a temporally-varying load by discretising the load into several steps. We see in Figure 6.1 that the load is constant over each time interval, and changes in steps between time intervals.
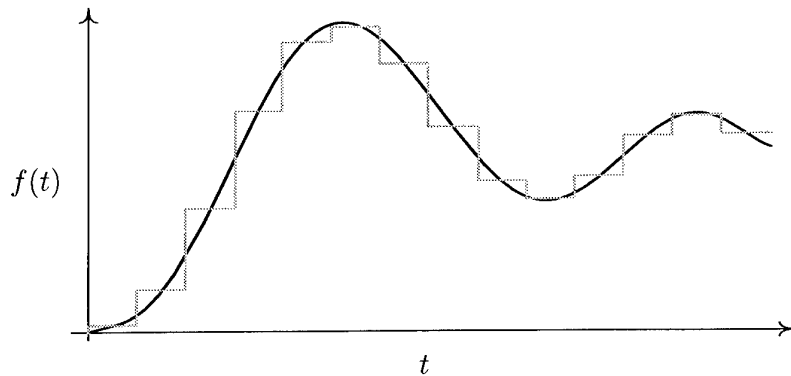
Figure 6.1: An example of how a continuous time-varying load $f(t)$ (black curve) can be discretised into steps (grey curve), thus allowing the use of the assumption of a "constant" loading distribution over each time interval.

7   Conclusion

After developing the non-dimensional partial differential equation governing the vibration of a cantilever beam, we solved the homogeneous form using the separation of variables technique.

In the main section of this report (§ 4), we showed that under certain circumstances we could predict the load distribution along a cantilever beam. For this load prediction we needed the initial deformation of the beam and either the strain response or the vibration response at *one* location along the beam. The reason we needed to know the initial deformation was that it and the strain (or vibration) response were related, and could not be separated without additional information. The need to know the initial deformation places a severe restriction on the practical implementation of the load prediction technique outlined in this report.

Using a finite element simulation we were able to verify our load prediction technique. As was expected, this simulation also demonstrated the effect noise might have on load prediction. Namely, noise corrupted the necessary information for the higher load mode determination. In contrast, the low load modes were seen to be robust.

Using a single measurement location to determine the load distribution along an entire beam, knowledge of the initial beam deformation was shown to be the most restrictive assumption. In operating conditions, the initial deformation of a helicopter rotor blade would be unknown, making the implementation of this load determination technique problematic. As such, it is suggested that no further consideration be given to this load determination approach using a single measurement location. Under normal operating conditions, multiple measurement locations would be required to determine the loading distribution along a rotor blade.

References

1. M. Abramowitz and I. A. Stegun, *Handbook of Mathematical Functions: with Formulas, Graphs, and Mathematical Tables*, Dover, 9th edn, 1972.

2. A. Arisio, S. Panizzi, and M. G. Paoli, *Inhomogeneous Timoshenko beam equations*, Mathematical Methods in the Applied Sciences, 15 (1992), pp. 621–630.

3. V. Barcilon, *On the solution of the inverse problem with amplitude and natural frequency data, I*, Phys. Earth Planet. Int., 13 (1976), pp. P1–P8.

4. ———, *On the multiplicity of solutions of the inverse problem for a vibrating beam*, SIAM J. Appl. Math., 37 (1979), pp. 605–613.

5. A. Berman, *System identification of structural dynamic models—theoretical and practical bounds*, in 25th Structures, Structural Dynamics and Materials Conference and AIAA Dynamics Specialist Conference, May 1984, pp. 123–129. (84-0929).

6. D. Boley and G. H. Golub, *Inverse eigenvalue problems for band matrices*, in Numerical Analysis, Proceedings of Biennial Conference on Numerical Analysis, G. A. Watson, ed., Springer-Verlag, 1977, pp. 23–31. (reference uncertain).

7. J. D'Cruz, *The Non-Linear Inverse Problem of Force Identification*, doctoral thesis, Department of Mechanical Engineering, Monash University, Clayton, Victoria 3168, Australia, 1991.

8. G. M. L. Gladwell, *The inverse problem for the vibrating beam*, Proc. R. Soc. Lond. Ser. A, 393 (1984), pp. 277–295.

9. ———, *Inverse problems in vibration II*, Applied Mechanics Reviews, 49 (1996), pp. 25–34.

10. G. H. Golub and C. F. Van Loan, *Matrix Computations*, Johns Hopkins, 1989.

11. S. Gopalakrishnan, M. Martin, and J. F. Doyle, *A matrix methodology for spectral analysis of wave propagation in multiple connected Timonshenko beams*, Journal of Sound and Vibration, 158 (1992), pp. 11–24.

12. M. D. Greenberg, *Applications of Green's Functions in Science and Engineering*, Prentice-Hall, 1971.

13. G. H. Hardy, *Divergent Series*, Clarendon, 1949.

14. S. G. Kelly, *Fundamentals of Mechanical Vibration*, McGraw-Hill, 1993.

15. K. Knopp, *Theory and Application of Infinite Series*, Dover, 1990. (Republication of English edition published by Blackie & Son, 1951.).

16. D. L. Kunz, *Survey and comparison of engineering beam theories for helicopter rotor blades*, Journal of Aircraft, 31 (1994), pp. 473–479.

17. D. M. LAUZON AND V. R. MURTHY, *Determination of vibration characteristics of multiple-load-path blades by a modified galerkin's method*, Computers and Structures, 46 (1993), pp. 1007–1020.

18. S. Y. LEE AND S. M. LIN, *Dynamic analysis of nonuniform beams with time-dependent elastic boundary conditions*, Journal of Applied Mechanics, 63 (1996), pp. 474–478.

19. L. MEIROVITCH, *Analytical Methods in Vibrations*, Macmillan, 1967.

20. ———, *Elements of Vibration Analysis*, McGraw-Hill, 2nd edn, 1986.

21. P. V. O'NEIL, *Advanced Engineering Mathematics*, Wadsworth, 2nd edn, 1987.

22. H. ÖRY, H. GLASER, AND D. HOLZDEPPE, *Reconstruction of forcing functions based on measured structural responses*, in Inter. Symp. on Aeroelasticity and Structural Dynamics (2nd: Aachen, West Germany), April 1985, pp. 656–668.

23. H. ÖRY AND H. W. LINDERT, *Reconstruction of spanwise air load distribution on rotorblades from structural flight test data*, in AAAF, 18th European Rotorcraft Forum, Avignon France, September 1992, pp. 74/1–12.

24. ———, *Reconstruction of rotor blade loading from in-flight measured structural blade reactions*, Acta Technica Acad. Sci. Hung., 105 (1993), pp. 301–326.

25. M. R. SPIEGEL, *Mathematical Handbook of Formulas and Tables*, Schaum's Outline Series, Schaum, 1968.

26. M. TANAKA AND A. N. BERCIN, *An integral equation formulation of the coupled vibration of uniform Timoshenko beams*, in Proceedings of the 19th International Conference on the Boundary Element Method, September 1997, pp. 127–136.

27. S. P. TIMOSHENKO AND J. M. GERE, *Theory of Elastic Stability*, McGraw-Hill, 2nd edn, 1961.

28. J. J. TUMA, *Engineering Mathematics Handbook: Definitions, Theorems, Formulas, and Tables*, McGraw-Hill, 2nd edn, 1987.

29. S. WOLFRAM, *The Mathematica Book*, Cambridge, 3rd edn, 1996. (Mathematica version 3.0).

30. W. C. YOUNG, *Roark's Formulas for Stress and Strain*, McGraw-Hill, 6th edn, 1989.

Index

accelerometer
    location, 12
assumption
    element rotation, 4
    length-height ratio ~, 4
    mass constant ~, 3
    periodic loading ~, 14
    separable solution ~, 5
    shear deformation ~, 4
    simple beam ~, 4
    sparse wrinkling ~, 4
    stiffness constant ~, 3
    temporally constant load ~, 11

beam
    distributed load, 3
    length, 3
    mass, 3
    verification ~, 17
bending moment, 3
boundary condition
    for 4th order DE, 5
    geometric ~, 3
    natural ~, 3

coefficient
    loading ~, 9
    solution ~, 9
constant
    4th order DE ~, 5
    hyperbolic ~, 5
    second order DE ~, 11
    separation of variables ~, 5

DE, *see* differential equation
differential equation, 5
discrete
    load, 10
        location, 10
        number of ~s, 10

error
    normalised ~, 21

FE, *see* finite element
finite element, 19
function

delta ~, 10
generalised ~, 12
hat, 13
impulse, *see* function, delta

initial
    displacement, 15
    velocity, 15
initial condition
    displacement ~, 4
    velocity ~, 4

load
    axial ~, 28

moment
    of inertia, *see* second moment of area
    second ~ of area, 3

Nastran, 19
natural frequency, 5

order, 7
orthogonal, 5
    functions, 9
orthonormal, 6

Parseval's identity, 22
partial differential equation, 1
PDE, *see* partial differential equation
precision
    loss of ~, 17

relative difference, 18
RMS, *see* root mean square
root mean square, 18, 24

separation of variables, 5
series, 7
shear force, 3
simulated
    strain, 20
spetra
    sympathetic ~, 1
stiffness, 3

Young's modulus, 3

Determining Beam Bending Distribution Using Dynamic Information

Frank G. Polanco

Number of Copies

AUSTRALIA

DEFENCE ORGANISATION

Task Sponsor

Director General Technical Airworthiness (ADF)	1

S & T Program

Chief Defence Scientist	
FAS Science Policy	
AS Science Corporate Management	1
Director General Science Policy Development	
Counsellor Defence Science, London	Doc Data Sht
Counsellor Defence Science, Washington	Doc Data Sht
Scientific Adviser to MRDC, Thailand	Doc Data Sht
Scientific Adviser Joint	1
Navy Scientific Adviser	Doc Data Sht
Scientific Adviser, Army	1
Air Force Scientific Adviser	1
Director Trials	1

Aeronautical and Maritime Research Laboratory

Director	1
Chief of Airframes and Engines Division	1
Research Leader Propulsion	1
Ken F. Fraser (Head of Helicopter Life Assessment)	1
Albert Wong (Task Manager)	1
Frank Polanco (Author)	1
Domenico C. Lombardo	1
Shane Dunn	1
Soon-Aik Gan	1

DSTO Libraries and Archives

Library Fishermans Bend	Doc Data Sht
Library Maribyrnong	Doc Data Sht
Library Salisbury	1
Australian Archives	1
Library, MOD, Pyrmont	Doc Data Sht
US Defense Technical Information Center	2
UK Defence Research Information Centre	2
Canada Defence Scientific Information Service	1
NZ Defence Information Centre	1
National Library of Australia	1

Capability Systems Staff

Director General Maritime Development	Doc Data Sht
Director General Aerospace Development	Doc Data Sht

Knowledge Staff

Director General, Control Communication and Computers	Doc Data Sht

Army

ASNSO ABCA, Puckapunyal	4
SO(Science), DJFHQ(L), MILPO Enoggera, Qld 4051	1
Commander Aviation Support Group, Oakey	1
NAPOC QWG Engineer NBCD c/- DENGRS-A, HQ Engineer Centre Liverpool Military Area, NSW 2174	Doc Data Sht

Air Force

Director General Technical Airworthiness (Attn OIC RWS), RAAF Williams	3

Intelligence Program

DGSTA Defence Intelligence Organisation	1
Manager, Information Centre, Defence Intelligence Organisation	1

Corporate Support Program

Library Manager, DLS-Canberra	1

Defence Material Organisation

Chief Engineer, Army Aircraft Logistics Management Squadron	1

UNIVERSITIES AND COLLEGES

Australian Defence Force Academy Library (ADFA)	1
Head of Aerospace and Mechanical Engineering, ADFA	1

Deakin University Library, Serials Section (M List), Geelong 3217	1
Monash University, Hargrave Library	Doc Data Sht
Librarian, Flinders University	1

OTHER ORGANISATIONS

NASA (Canberra)	1
AusInfo	1

OUTSIDE AUSTRALIA

ABSTRACTING AND INFORMATION ORGANISATIONS

Library, Chemical Abstracts Reference Service	1
Engineering Societies Library, US	1
Materials Information, Cambridge Science Abstracts, US	1
Documents Librarian, The Center for Research Libraries, US	1

INFORMATION EXCHANGE AGREEMENT PARTNERS

Acquisitions Unit, Science Reference and Information Service, UK	1
Library – Exchange Desk, National Institute of Standards and Technology, US	1
Inderjit Chopra, Minta-Martin Professor and Director, Alfred Gessow Rotorcraft Center, Aerospace Engineering, University of Maryland, Maryland	1
Charlie Crawford, Chief Engineer, Aerospace and Transportation Laboratory, Georgia Tech Research Institute, Alabama	1
Prof Phil Irving, Head Damage Tolerance Group, School of Industrial and Manufacturing Science, Cranfield University, Cranfield	1

U.S. Army

Felton Bartlett, US Army Research Laboratory, NASA Langley Research Center (Virginia)	1
Kevin Rotenberger, Aviation and Missile Command (Redstone Arsenal, Alabama)	1
SPARES	5

Total number of copies: 59

DEFENCE SCIENCE AND TECHNOLOGY ORGANISATION DOCUMENT CONTROL DATA		1. CAVEAT/PRIVACY MARKING	

2. TITLE Determining Beam Bending Distribution Using Dynamic Information	3. SECURITY CLASSIFICATION Document (U) Title (U) Abstract (U)		

4. AUTHOR Frank G. Polanco	5. CORPORATE AUTHOR Aeronautical and Maritime Research Laboratory 506 Lorimer St, Fishermans Bend, Victoria 3207, Australia		

6a. DSTO NUMBER DSTO–RR–0226	6b. AR NUMBER AR–012–097	6c. TYPE OF REPORT Research Report	7. DOCUMENT DATE January, 2002

8. FILE NUMBER M1/9/583	9. TASK NUMBER NAV 01/124	10. SPONSOR DGTA	11. No OF PAGES 32	12. No OF REFS 30

13. URL OF ELECTRONIC VERSION http://www.dsto.defence.gov.au/corporate/ reports/DSTO–RR–0226.pdf	14. RELEASE AUTHORITY Chief, Airframes and Engines Division

15. SECONDARY RELEASE STATEMENT OF THIS DOCUMENT

Approved For Public Release

OVERSEAS ENQUIRIES OUTSIDE STATED LIMITATIONS SHOULD BE REFERRED THROUGH DOCUMENT EXCHANGE, PO BOX 1500, SALISBURY, SOUTH AUSTRALIA 5108

16. DELIBERATE ANNOUNCEMENT

No Limitations

17. CITATION IN OTHER DOCUMENTS

No Limitations

18. DEFTEST DESCRIPTORS

bending; vibration; cantilever beams; loads (forces); aerodynamic loads; finite element analysis; strain measurement; vibration tests; vibration mode; or modes; background noise

19. ABSTRACT

As a first approximation, a helicopter rotor blade may be modelled as a cantilever beam. Given the initial deformation of this beam, and using either strain or acceleration at one location along the beam, we can determine the load distribution along the entire beam. We consider load distributions that can vary spatially, but are constant in time (except for the initial step input). In the solution we neglect the effects of both aerodynamic and mechanical damping. The separation of variables technique leads to a solution in terms of the beam's natural modes. The loading distribution is decomposed in terms of these modes. A finite element simulation of the beam's response to a cubic load distribution verifies that this load prediction is possible. We demonstrate that the higher modes of the load prediction are unstable when noise is present in the measurements, but that the lower modes are robust. If the initial beam deformation is unknown, then additional (strain or vibration) measurement locations may be substituted for the unknown initial deformation.